Bioactive Materials 24 (2023) 313–321

Contents lists available at ScienceDirect

Bioactive Materials

journal homepage: www.keaipublishing.com/en/journals/bioactive-materials

Melanin nanoparticles alleviate sepsis-induced myocardial injury by suppressing ferroptosis and inflammation

Chang Liu [a,c,1], Quan Zou [d,1], Huixin Tang [a,1], Jia Liu [a], Shiqi Zhang [a], Caihong Fan [a], Junwei Zhang [b], Ruiqing Liu [a], Yashan Liu [a], Ruiyan Liu [a], Yan Zhao [a], Qiang Wu [c], Zhi Qi [b,e,f,**], Yanna Shen [a,c,*]

[a] School of Medical Technology, Tianjin Medical University, Tianjin, 300203, China
[b] Department of Molecular Pharmacology, School of Medicine, Nankai University, Tianjin, 300071, China
[c] Key Laboratory of Emergency and Trauma of Ministry of Education, Hainan Medical University, Haikou, 571199, China
[d] Department of Radiology, The Second Hospital of Tianjin Medical University, Tianjin, 300211, China
[e] Tianjin Key Laboratory of General Surgery in Construction, Tianjin Union Medical Center, Tianjin, 300000, China
[f] Xinjiang Production and Construction Corps Hospital, Xinjiang, 830092, China

ARTICLE INFO

Keywords:
Sepsis
Myocardial injury
Melanin nanoparticles
Ferroptosis
Inflammation

ABSTRACT

Myocardial injury as one of the severe complications leads to the increasing morbidity and mortality in patients with sepsis. Recent studies reported that reactive oxygen species (ROS)-mediated ferroptosis plays a critical role in the development of heart diseases. Therefore, we hypothesized that anti-ferroptosis agent might be a novel potential therapeutic strategy for sepsis-induced cardiac injury. Herein, we demonstrated that a small biocompatible and MRI-visible melanin nanoparticles (MMPP) improves myocardial function by inhibiting ROS-related ferroptosis signaling pathway. In LPS-induced murine sepsis model, after a single dose intravenously injection of MMPP treatment, MMPP markedly alleviated the myocardial injury including cardiac function and heart structure disorder through suppressing iron-accumulation induced ferroptosis. *In vitro*, MMPP inhibited cardiomyocyte death by attenuating oxidative stress, inflammation and maintaining mitochondrial homeostasis. Collectively, our findings demonstrated that MMPP protected heart against sepsis-induced myocardial injury via inhibiting ferroptosis and inflammation, which might be a novel therapeutic approach in future.

1. Introduction

Myocardial injury is the most common and severe complication of sepsis, which is considered as a predictor of mortality [1,2]. According to statistics, more than 50% of patients with sepsis have different degrees of cardiac dysfunction in the early stage [3]. The mortality rate of patients with sepsis but without myocardial injury is 20%, in contrast, the mortality rate of patients with myocardial injury reaches as high as 70%–90% [4,5]. However, the mechanisms underlying sepsis-induced cardiac injury still remain unclear and the current clinical therapy effects are very limited. Although it is commonly considered that programmed cardiomyocyte death, such as pyroptosis, autophagy, or apoptosis, is a vital pathological feature in the process of cardiac injury [6–8]. Sepsis-induced cardiac injury could not be alleviated completely after inhibiting these deaths by various approaches, indicating that other types of cell death may contribute to this process (see Scheme 1).

Ferroptosis, different from apoptosis, pyroptosis and autophagy, is a novel programmed cell death triggered by imbalanced iron homeostasis and lipid peroxidation, [9–11]. Since its discovery, ferroptosis has been shown to be associated with the pathologic process of numerous cardiovascular diseases, such as sepsis-induced myocardial injury, myocardial infarction, diabetic cardiomyopathy and cardiac ischemia-reperfusion [12–15]. In sepsis-induced myocardial injury, overproduction of ROS can promote inflammation, oxidative stress, lipid peroxidation, and lead to cardiomyocyte ferroptosis [16–18]. However, excessive inflammatory cytokines, including interleukin-1β, tumor

Peer review under responsibility of KeAi Communications Co., Ltd.
* Corresponding author. School of Medical Technology, Tianjin Medical University, Tianjin, 300203, China.
** Corresponding author. Department of Molecular Pharmacology, School of Medicine, Nankai University, Tianjin, 300071, China.
E-mail addresses: qizhi@nankai.edu.cn (Z. Qi), shenyanna@tmu.edu.cn (Y. Shen).
[1] These authors contributed equally to this work.

https://doi.org/10.1016/j.bioactmat.2022.12.026
Received 25 August 2022; Received in revised form 23 December 2022; Accepted 23 December 2022

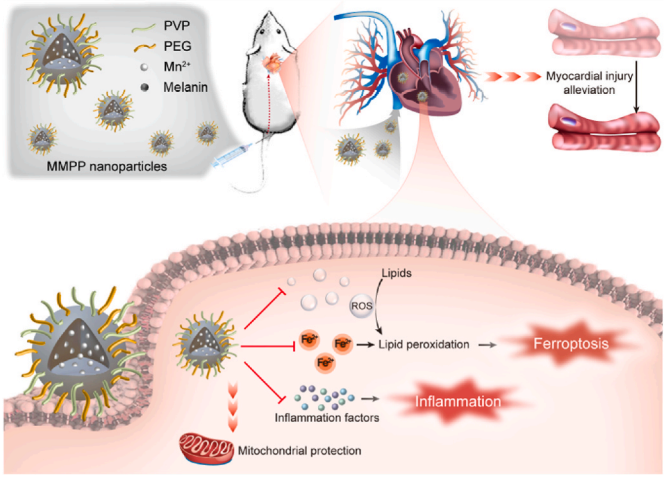

Scheme 1. Schematic illustration of the treatment and mechanism of MMPP nanoparticles for sepsis-induced myocardial injury.

necrosis factor-α and interleukin-6 also result in production of ROS and activation of oxidative stress, which in turn causes cardiomyocyte death through ferroptosis [19–21]. Recently, Li et al. reported that ferroptosis inhibitors Ferrostatin-1 and Dexrazoxane effectively alleviated cardiac injury in sepsis mice by inhibiting ferroptosis [9]. These findings raise the possibility that specific targeting of ferroptosis may be a promising approach for clinical treatment of myocardial injury caused by sepsis.

Melanin is a kind of endogenous biomolecules in various living organisms, which exhibits inherent biocompatibility and is widely used for biomedical applications, including UV irradiation protection, cancer and anti-infective therapy [22–26]. Due to its free phenolic properties of melanin and ability to scavenger a variety of reactive oxygen and nitrogen species, artificial melanin-like nanoparticles have been widely applied to antioxidant treatment of many ROS-related diseases, such as myocardial infarction, ischemia/reperfusion injury, acute kidney and lung injury [27–30]. Moreover, melanin-like nanoparticles also exhibited great chelating capability to different types of metal ions due to the phenolic hydroxyl and amine groups on their surface [31–36]. Recently, Zhao et al. found that melanin-like nanoparticles can strongly inhibit LPS-induced inflammation, which is promising as an anti-inflammatory nano drug for the treatment of inflammatory diseases [29]. However, the application of melanin-like nanoparticles as an anti-ferroptosis and anti-inflammation strategy to treat sepsis-induced myocardial injury remains unavailable.

In this study, we synthesized polyethylene glycol and polyvinylpyrrolidone modified Mn^{2+}-chelated melanin (MMPP) nanoparticles and explored both its potential therapeutic effect and molecular mechanism as a nano-drug in the treatment of sepsis-induced myocardial injury via anti-ferroptosis and anti-inflammation. In a mice model of LPS-induced sepsis, we observed that intravenously injection of MMPP improved mice survival rate and cardiac function through suppressing iron accumulation induced ferroptosis. Additionally, we revealed that MMPP were able to significantly alleviate the oxidative stress and inflammation response *in vitro*, as evidenced by the attenuation of ROS and inflammatory cytokines production. Furthermore, we demonstrated that treatment with MMPP effectively maintained mitochondrial homeostasis. Our study proposed that such accessible, safe and multifunctional biomaterials might be a therapeutic choice for clinical treatment of sepsis-induced myocardial injury.

2. Material and methods

2.1. Reagents and materials

All chemicals used were at least analytical grade. Melanin and manganese chloride tetrahydrate ($MnCl_2{\cdot}4H_2O$) were obtained from Sigma-Aldrich (St. Louis, MO, USA). Polyvinylpyrrolidone (PVP; average MW: 10 kDa), Thiol-terminated poly (ethylene glycol) (HS-PEG, average MW: 5 kDa) and ammonium hydroxide solution (28 wt%) were purchased from Aladdin Reagent Co., Ltd. (Shanghai, China). Dimethyl sulfoxide (DMSO) was obtained from Tianjin Concord Technology (Tianjin, China). MDA assay kit (A3003-1-2) and Iron assay kit (A039-2-1) were purchased from Nanjing Jiancheng Bioengeneering Institute (Nanjing, China). LDH (BC085) and SOD assay kit (BC0170) was purchased from Solarbio (Beijing, China).

2.2. Synthesis of MMPP nanoparticles

The MMPP nanoparticles were synthesized according to the previous study [30]. Mn-Melanin-PVP (MMP) nanoparticles were firstly synthesized. Melanin was dissolved in DMSO (1 mg/mL, 5 mL) under 25 °C water bath with stirring. Then 5 mL of DMSO containing 18 mg of $MnCl_2{\cdot}4H_2O$ and 50 mg of PVP was added, followed by continuous stirring for 12 h. Subsequently, the mixture was added to 100 mL H_2O under stirring. The MMP nanoparticles were purified by centrifugal ultrafiltration (30 kDa molecular weight cut off) with deionized water for several times.

MMPP nanoparticles were synthesized via the modification of MMP with HS-PEG. HS-PEG was dissolved in H_2O (10 mg/mL, 5 mL) with stirring. The pH of MMP solution (2 mg/mL, 5 mL) was adjusted to 9.5 with ammonium hydroxide solution, and dropwise added to the HS-PEG solution under stirring and argon gas protection, followed by continuous stirring for 12 h at room temperature. The MMPP nanoparticles were purified by centrifugal ultrafiltration (30 kDa molecular weight cut off) with deionized water for several times. The MMPP nanoparticles were stored at 4 °C for further experiments. For the synthesis of Melanin-PVP-PEG nanoparticles, the $MnCl_2{\cdot}4H_2O$ did not added to the reaction. Other reaction steps were the same as those of MMPP synthesis.

2.3. Characterization

The morphology of the MMPP nanoparticles were characterized by a Philips Tecnai G2 F20 microscope with an accelerating voltage of 200 kV (HRTEM, Philips, Holland). Hydrodynamic size and zeta potential of MMPP nanoparticles were measured by a Malvern Zetasizer (Nano series ZS90, UK). The FTIR spectra (400–4000 cm^{-1}) of the materials were obtained on a Nicolet IS 10 spectrometer with pure KBr as the background (Thermo Scientific, USA).

2.4. ROS-scavenging capacity of MMPP nanoparticles

ABTS radical scavenging capacity. The free radical scavenging capability of MMPP nanoparticles was tested based on the ABTS radical cation decolorization assay. First, the ABTS radical solutions were prepared by mixing 7 mM ABTS solution with 2.45 mM potassium persulfate for 16 h in the dark. Then, the MMPP solution or Melanin-PVP-PEG solution was mixed with ABTS radical solution (final concentration 0, 5, 10, 20, 30, 40, 50, 75, 100 mg/L), and incubated for 10 min. The corresponding MMPP solution or Melanin-PVP-PEG solution without ABTS radical solution was used for deduction of the background absorbance. The absorbance of the mixture at 734 nm was measured by a microplate reader (BioTeK, USA). The inhibition rate of ABTS radicals was calculated by the following equation: the inhibition rate (%) = $((A_{ABTS}-A_{Sample}-A_{MMPP})/A_{ABTS}) \times 100\%$. A_{ABTS} means the absorbance of pure ABTS radical solution at 734 nm. A_{sample} refers to the 734 nm absorbance of ABTS radical solution with MMPP. A_{MMPP} is the 734 nm absorbance of

pure MMPP solution.

Hydroxyl radical (·OH) scavenging capacity. The ·OH scavenging capacity of MMPP nanoparticles at different concentrations (0, 40, 70, 100, 150 and 200 mg/L) was tested with a hydroxyl radical assay kit (Nanjin Jiancheng Bioengineering Institute, China).

Superoxide anion radical ($O_2\cdot^-$) scavenging capacity. The $O_2\cdot^-$ scavenging capacity of MMPP nanoparticles at different concentrations (0, 100, 200, 400, 700 and 1000 mg/L) was tested with a total superoxide dismutase assay kit with WST-8 method (Beyotime Biotechnology, China).

2.5. Iron-chelating capacity of MMPP nanoparticles

The 1,10-phenanthroline was used to determine the iron-chelating capacity of MMPP nanoparticles. Various concentrations of MMPP solution (0, 100, 200, 350 and 500 mg/L) were incubated with 50 μM $FeCl_2$ solution at room temperature. After 1 h, 1,10-phenanthroline solution were added with the final concentration of 300 μM, and the absorbance of the mixture at 510 nm was measured by a microplate reader (BioTeK, USA). The corresponding MMPP/1,10-phenanthroline solution without the addition of $FeCl_2$ was used for deduction of the background absorbance.

2.6. Longitudinal relaxivity and T_1-weighted MR imaging

Longitudinal relaxivity. The longitudinal relaxivity time and T_1-weighted images of MMPP solution with different Mn concentrations (0.00, 0.01, 0.25, 0.05, 0.1, 0.15, 0.20 mmol/L) were acquired via a 1.2 T small MR imaging system (HT/MRSI60-60KY, Shanghai Huantong, China). Longitudinal relaxivity (r_1) of MMPP nanoparticles was obtained by linear fitting of $1/T_1$ versus Mn concentration.

In vivo MR imaging. In vivo MR imaging of C57BL/6J mice was carried out on a clinical GE MR 750 system (GE Signa Excite). Typically, C57BL/6J mice were anesthetized (1.5% isoflurane) and intravenously injected with MMPP solution (10 mg/mL, 100 μL). T_1-weighted MR images of mice before and after MMPP injection were obtained at desired time intervals. Imaging parameters, slice thickness = 1 mm, slice spacing = 0.5 mm, repetition time (TR) = 360 ms, echo time (TE) = 13.38 ms.

2.7. Animals and models

C57BL/6J adult male mice weighing 18 g–20 g and aged 7–8 weeks were purchased from Sipeifu (Beijing, China). All mice were housed in the SPF animal room with free access to water and food. The mice were randomly divided into 3 groups: Control group, LPS group and LPS + MMPP group. The sepsis-induced cardiac injury model was established by receiving a single intravenously injection with lipopolysaccharide (LPS) at a dose of 10 mg/kg for 12 h. The mice in LPS + MMPP group were injected intravenously with MMPP (100 μL, 10 mg/mL) after 30 min LPS injection. Control group mice were intravenously injected with sterile PBS at the same dose. Twelve hours after LPS injection, mice were performed echocardiography or collected blood from heart and heart tissue for analysis. All animal experiments were approved by the Experimental Animal Ethics Committee of Tianjin Medical University.

2.8. Biodistribution and in vivo toxicity of MMPP nanoparticles

For biodistribution study, health C57BL/6J mice and LPS-induced sepsis mice were intravenously injected with MMPP solution (10 mg/mL, 100 μL), and sacrificed at different time points of 10 min, 1 h, 6 h, 12 h and 24 h. Main organs including heart, liver, spleen, lung, and kidney were harvested, and digested respectively with aqua regia for determination of Mn content by inductively coupled plasma-mass spectrometry (ICP-MS).

For biotoxicity study, C57BL/6J mice were divided into four groups randomly (n = 4, each group). One group (control) was intravenously injected with PBS (100 μL). Three groups were intravenously injected with MMPP solution (10 mg/mL, 100 μL) and sacrificed on 1 h, 1 day and 14 days post injection, respectively. The main organs including heart, liver, spleen, lung and kidney were dissected for histopathological examination. The blood samples were collected from the sacrificed mice, biomarkers of liver function and kidney function in the serum were determined with an automatic biochemical analyzer (AU5800 auto-analyzer, Beckman Coulter Inc., Brea, CA, USA).

2.9. Cell culture

Neonatal rat ventricle cardiomyocytes were obtained from ventricles of 1-day-old Sprague Dawley rats (SPF Biotechnology Co. Ltd). Ventricular tissue was minced into smaller pieces and digested using 1% trypsin (Rhawn) at 4 °C overnight and further digested in 0.25% collagenase II (Worthington). After aggregated tissue was removed by filtration, cells were then pre-plated for 4 h to remove non-myocytes. The primary cardiomyocytes were cultured in DMEM (Gibco) supplemented with 7% FBS (Lonsera) and 1% streptomycin/penicillin (Solarbio) for 24 h. The medium was then removed, and cardiomyocytes were cultured in DMEM (Gibco) supplemented with 1% transferrin (Basal Media) and 1% streptomycin/penicillin (Solarbio) for 24 h before LPS or MMPP treatment.

2.10. Western blot and real-time PCR assay

Western blot and real-time PCR assay were performed as previously published article described [37]. Rabbit anti-PTGS2 (A1253) (Western blot, 1: 1000) and anti-GAPDH (AC002) (Western blot, 1: 2000) were purchased from ABclonal (Wuhan, China). The primers used in our study were listed in Supplementary Table 1.

2.11. Echocardiography

Twelve hours after LPS injection, the mouse echocardiography was performed under anesthesia (1.5% isoflurane). To calculate cardiac function, the heart rate, LV ejection fraction (EF%) and LV fractional shortening (FS%) were collected from three to five consecutive cardiac cycles.

2.12. Cell fractionation assay

According to the manufacturer's instructions (C3601, Beyotime), the cells were resuspended in the separation buffer and homogenized by repeated douncing. The cells were centrifuged at 1000 g for 10 min at 4 °C, and then supernatants were collected to centrifuge at 11,000 g for 10min at 4 °C. The precipitates were mitochondria and the supernatants were cytoplasm.

2.13. Measurement of MDA, SOD and iron

The tissue and intracellular MDA, SOD and iron were measured using commercial assays kits according to the manufacturer's instruction.

2.14. Measurement of intracellular ROS

Cells were incubated with serum-free medium containing DCFH-DA fluorescent probe at 37 °C for 40 min. Then, cells were washed with PBS for three times. Results were expressed as green fluorescence intensity, which represented intracellular ROS level.

2.15. Measurement of lipid ROS

The cells were seeded in 6-well plates and pretreated with LPS and MMPP as previously described, and then incubated with 5 μM (work

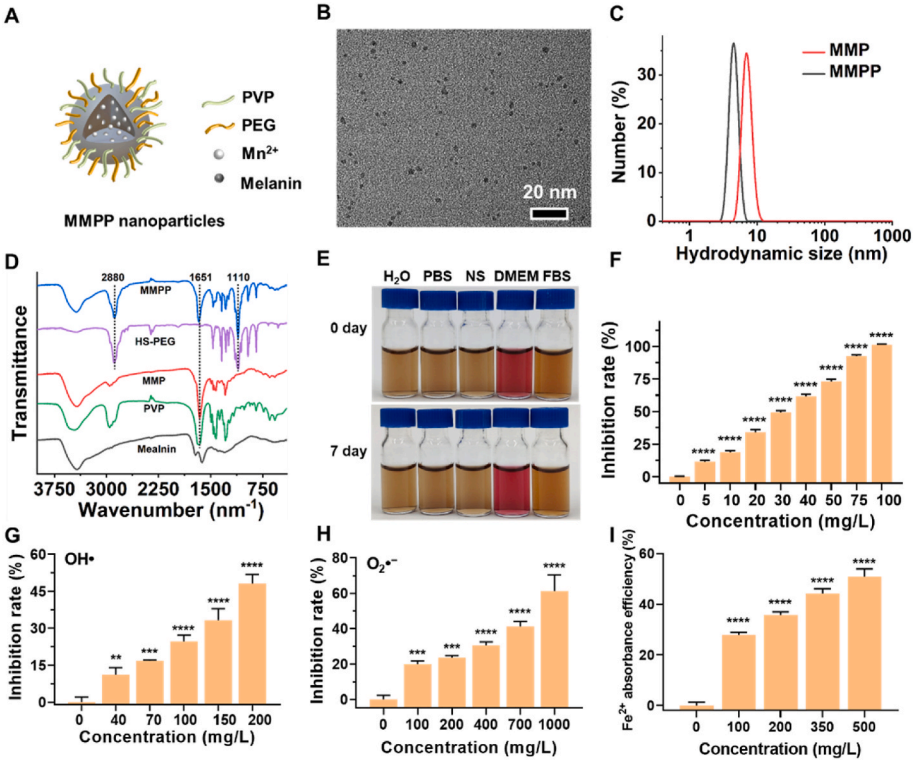

Fig. 1. Synthesis and characterization of MMPP nanoparticles. (A) Schematic diagram of MMPP nanoparticles. (B) TEM image of MMPP nanoparticles. (C) Hydrodynamic diameter distribution of MMPP nanoparticles and MMP nanoparticles on the DLS measurement. (D) FTIR spectra of MMPP nanoparticles, HS-PEG molecule, MMP nanoparticles, PVP molecule and melanin granules. (E) Photos of MMPP nanoparticles dispersed in different media including H_2O, phosphate buffered saline (PBS), normal saline (NS), Dulbecco's Modified Eagle Medium (DMEM) and fetal bovine serum (FBS) and for 7 days. (F) Antioxidant capacity of MMPP nanoparticles by the ABTS method. (G) OH• and (H) $O_2^{\bullet -}$ scavenging activity of MMPP nanoparticles. (I) Iron chelation efficiency of MMPP nanoparticles. Data are presented as mean ± SD. $^{**}p < 0.01$, $^{***}p < 0.001$, $^{****}p < 0.0001$ vs. 0 mg/L group.

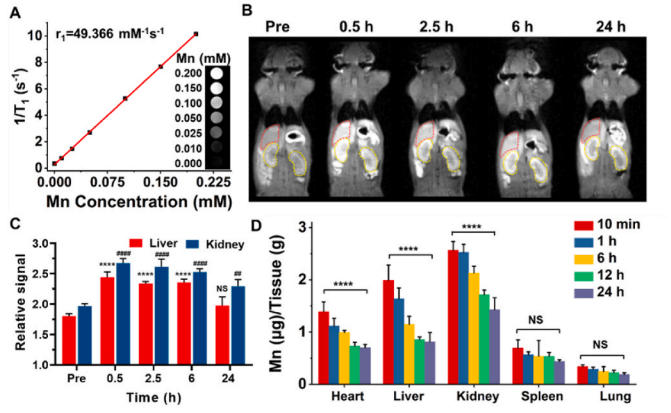

Fig. 2. MR Imaging performance and biodistribution of MMPP nanoparticles. (A) Longitudinal relaxivity of MMPP nanoparticles. Insert, T_1-weighted images of MMPP nanoparticles at different Mn concentrations. (B) T_1-weighted images and (C) corresponding relative T_1 signal of liver and kidneys of C57BL/6J mice before and after intravenous injection of MMPP nanoparticles (10 mg/mL, 100 μL). The red and yellow irregular circles point to the liver and kidneys, respectively. Data are presented as mean ± SD. $^{****}p < 0.0001$ vs. liver pre. $^{\#\#\#\#}p < 0.0001$ vs. kidney pre. (D) Biodistribution of Mn in major organs (heart, liver, kidney, spleen, and lung) of health C57BL/6J mice. Data are presented as mean ± SD. $^{****}p < 0.0001$. NS means not significant.

concentration) BODIPY 581/591 C11 (D3861, Invitrogen, USA) probe in the dark. After 30 min, cells were washed with PBS for three times and then acquired images by fluorescence microscope.

2.16. Statistical analysis

Statistical significance was calculated by performing one-way ANOVA followed by Dunnett post hoc test for the comparison of three or more groups with one variable, using Prism software (GraphPad, San Diego, CA). All p values less than 0.05 were considered to be statistically significant.

3. Results

3.1. Synthesis and characterization of MMPP nanoparticles

The MMPP nanoparticles were easily prepared according to the reported method [30]. The melanin is a granular powder with intrinsic poor water-solubility (Figs. S1A and S1B), which could be broken down into nanoscale through a simple coordination and self-assembly method, followed by thiol-terminated polyethylene glycol (HS-PEG) modification (Fig. 1A). The as-prepared Mn-Melanin-PVP (MMP) and MMPP nanoparticles showed good monodispersity (Fig. 1B and Fig. S1C). The average hydrodynamic size of MMPP nanoparticles was 4.517 ± 0.576 nm, which is a little smaller than MMP nanoparticles (7.12 ± 1.023 nm) (Fig. 1C). The zeta potential of MMPP nanoparticles was −2.30 mV. The characteristic peaks of PVP at 1651 cm^{-1} (C═O stretching vibration), and PEG at 2880 cm^{-1} and 1110 cm^{-1} (alkyl C–H stretching vibration and C–O–C stretching vibration) all appeared in the spectrum of MMPP nanoparticles, demonstrating the successful functionalization of melanin with PVP and HS-PEG (Fig. 1D) [30]. The MMPP nanoparticles were dispersed in water, phosphate buffered saline (PBS) (10 mM, pH 7.4), normal saline (NS), Dulbecco's Modified Eagle Medium (DMEM) and fetal bovine serum (FBS). There were no aggregates observed in various media, and the hydrodynamic size did not change obviously in 7 days, demonstrating the good colloidal stability of MMPP nanoparticles (Fig. 1E and Fig. S1D).

3.2. ROS-scavenging and iron-chelating capacity of MMPP nanoparticles

The ROS-scavenging capacity of MMPP nanoparticles was systematically evaluated. Firstly, the antioxidant capability of MMPP nanoparticles was investigated using 2,2′-azino-bis-3-ethylbenzthiazoline-6-sulfonic acid radical ($ABTS^{\cdot +}$) eliminating method. MMPP nanoparticles could notably scavenge the $ABTS^{\cdot +}$ in a concentration-dependent manner (Fig. 1F). Almost 100% of $ABTS^{\cdot +}$ was scavenged by MMPP

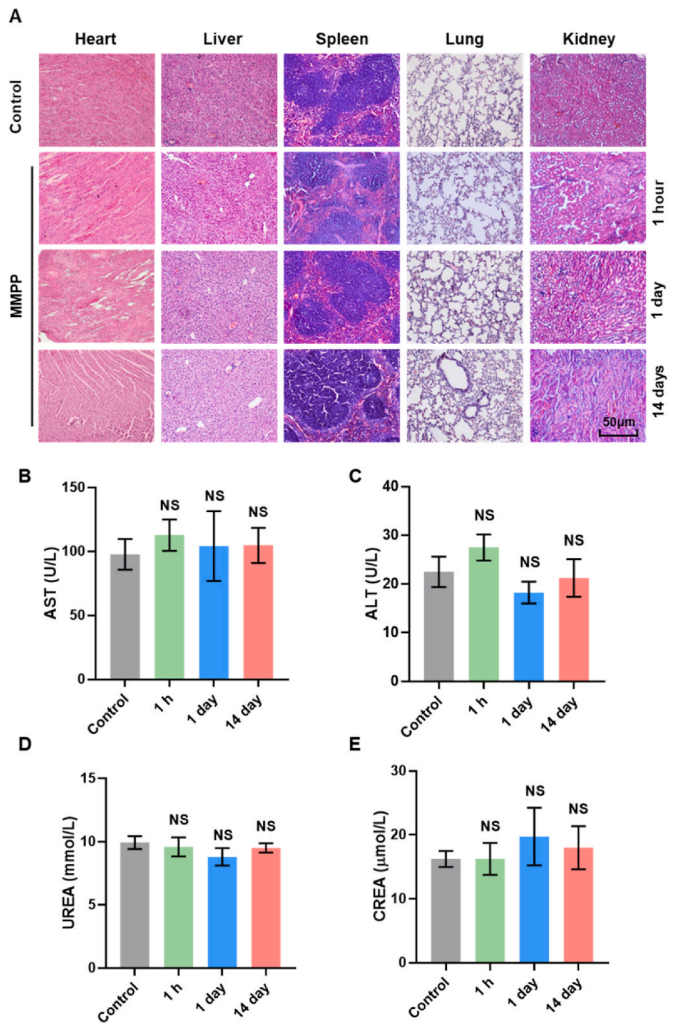

Fig. 3. *In vivo* biosafety validation of MMPP nanoparticles. (A) H&E staining images of the major organs (heart, liver, spleen, lung, and kidney) collected from the mice after intravenous injection of MMPP for 1 h, 1day, and 14 days (10 mg/mL, 100 μL). Scale bar = 50 μm. (B–E) Blood biochemical analysis of mice at 1 h, 1day, and 14 days after intravenous administration of MMPP (10 mg/mL, 100 μL). Data are presented as mean ± SD. NS means not significant.

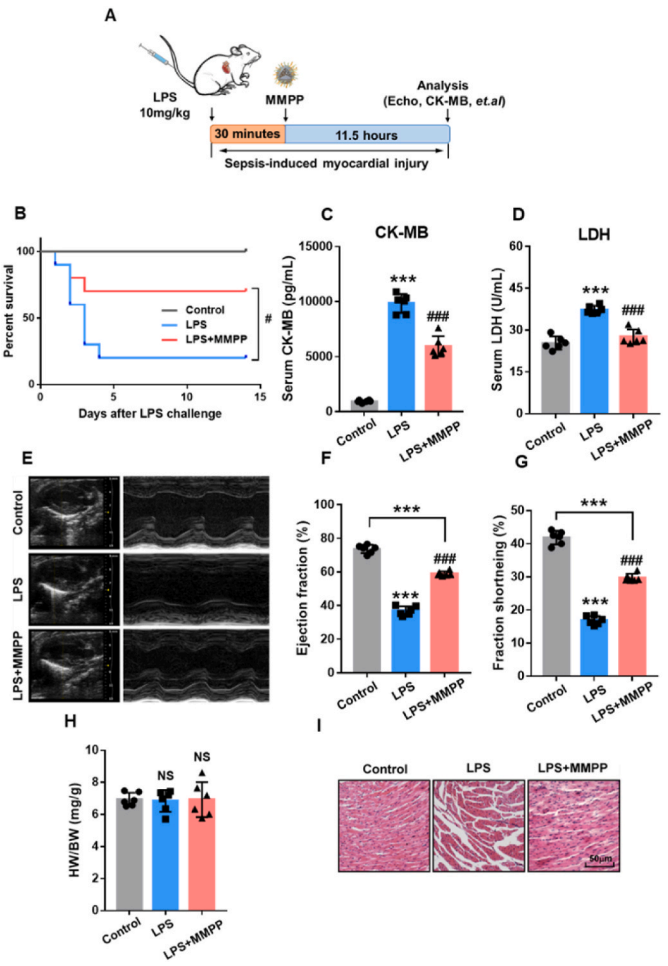

Fig. 4. MMPP treatment improved survival and cardiac function in LPS-induced sepsis mice. (A) Schematic illustration of the establishment of the sepsis-related myocardia injury mouse model. (B) The 14-day survival rate was observed after MMPP treatment. (C–D) The serum CK-MB and LDH content were measured by their respective kits. (E) Representative M-mode echocardiographs from control mice and LPS-induced mice treated with PBS or MMPP nanoparticles. (F–G) Quantitative analysis of the ejection fraction and fractional shortening. (H) HW/BW ratio from mice in each group. (I) Representative H&E staining images of the heart tissue from mice in each group. Scale bar = 50 μm. Data are presented as mean ± SD.$^{***}p < 0.001$ vs. non-infection control group, $^{###}p < 0.001$ vs. LPS infection control group. NS means not significant.

nanoparticles at a low concentration of 100 mg/L. Meanwhile, the Mn^{2+} free Melanin-PVP-PEG nanoparticles also showed the similar $ABTS^{\cdot+}$ scavenge capacity compared with MMPP (Fig. S1E). Then, the capability of MMPP nanoparticles on eliminating other ROS, hydroxyl radical (·OH) and superoxide anion radical ($O_2^{\cdot-}$), was further investigated. The results showed that ·OH and $O_2^{\cdot-}$ could be effectively scavenged in a concentration-dependent manner. The clearance rates of ·OH reached 48.14% at 200 mg/L of MMPP nanoparticles, and $O_2^{\cdot-}$ reached 61.24% at 1000 mg/L of MMPP nanoparticles (Fig. 1G and H). All above results indicated the admirable ROS-scavenging capacity of MMPP nanoparticles toward various ROS *in vitro*.

As the melanin possesses a lot of phenolic hydroxyl groups, it is reasonable to test the iron-chelating capacity of MMPP nanoparticles. The 1,10-phenanthroline could coordinate with Fe^{2+} and form an orange-red complex with high absorbance at 510 nm. There was a good linear relationship between 510 nm absorption of 1,10-phenanthroline-Fe^{2+} complex and Fe^{2+} concentration (0–50 μM), which proved that 1,10-phenanthroline can be used as indicator to sensitively detect free Fe^{2+} (Fig. S1F). When different concentrations of MMPP solution incubated with 50 μM Fe^{2+} for 1 h, the concentration of free Fe^{2+} was decreased obviously with a concentration-dependent manner (Fig. 1I).

The Fe^{2+} chelating efficiency reached 51.0% after incubation with 500 mg/L MMPP solution, demonstrating the good iron-chelating capacity of MMPP nanoparticles.

3.3. MR imaging performance and biodistribution of MMPP nanoparticles

The Mn^{2+} of MMPP has unpaired electrons, which could shorten the longitudinal relaxation time of surrounding hydrogen protons and can be used for T_1-weighted MR imaging. To assess the capacity of MMPP nanoparticles as a contrast agent for MR imaging, T_1 relaxivity and T_1-weighted MR imaging were carried out *in vitro*. The T_1 relaxivity of MMPP could reach 49.366 $mM^{-1}s^{-1}$, which is much higher than clinically used T_1 contrast agent (Gd-DTPA, 4.6 $mM^{-1}s^{-1}$), and the MR images of MMPP showed an obvious concentration-dependent brightening effect (Fig. 2A). Subsequently, MMPP nanoparticles were intravenous injected to C57BL/6J mice and T_1-weighted MR images were acquired at different time points. After MMPP nanoparticles were intravenously injected, a significant enhancement of liver and kidney could be

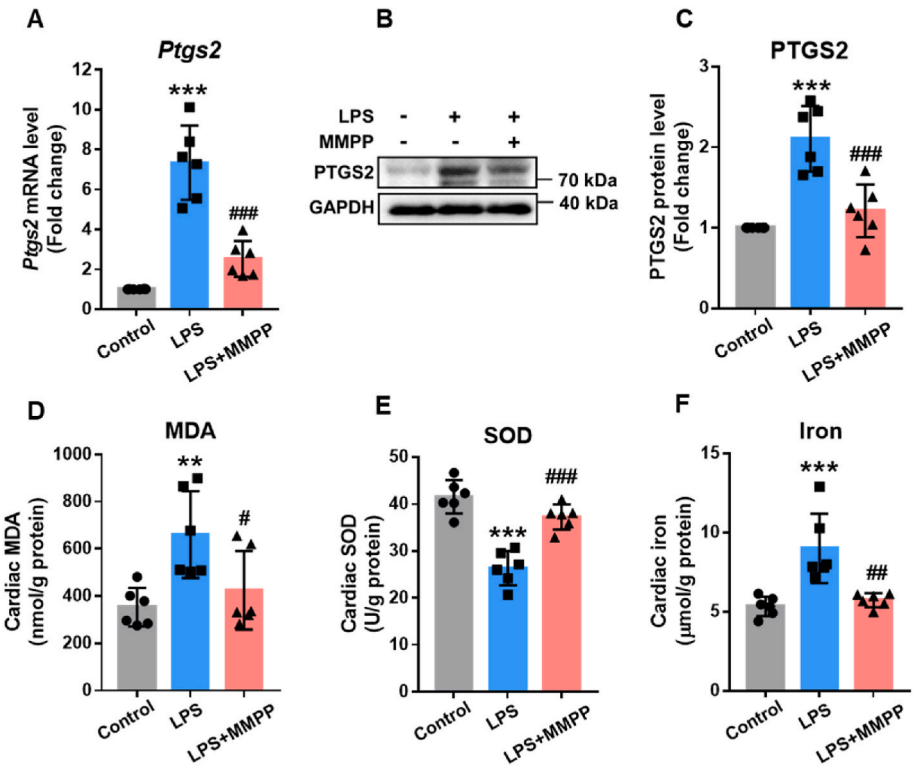

Fig. 5. MMPP inhibited ferroptosis *in vivo* by chelating iron. A-F. The mice were given 10 mg/kg LPS, and MMPP was administered 30 min after LPS challenge. Cardiac tissues were collected 12h after LPS challenge. (A) The mRNA expression of gene in mouse heart tissue was measured by RT-PCR. (B–C) Immunoblots and quantitative analysis of PTGS2/GAPDH in heart tissue. (D–F) The MDA, SOD and iron contents were examined by their respective kits. Data are presented as mean ± SD. $^{**}p < 0.01$, $^{***}p < 0.001$ vs. non-infection control group, $\#p < 0.05$, $\#\#p < 0.01$, $\#\#\#p < 0.001$ vs. LPS infection control group.

observed at 0.5 h post-injection (Fig. 2B and C). As time went on, the signal of liver and kidney started to weaken, and only a slight enhancement were observed at 24 h post injection. Meanwhile, the bladder also showed an enhancement at 0.5 h and 2 h after injection (Figs. S2A and S2B). All above results indicated that the MMPP could metabolize by both liver and kidney.

Though the MR imaging revealed general metabolism information of MMPP nanoparticles, it still meaningful to study the MMPP biodistribution in detail. The mice treated with MMPP nanoparticles were sacrificed at specific time points, and the major organs (heart, liver, spleen, lung and kidney) were collected, weighed and digested with aqua regia for ICP-MS determination of Mn concentrations. As expected, high levels of Mn contents mainly accumulated in liver and kidney, and constantly decreased over time, which is consistent with the MR imaging results (Fig. 2D). Meanwhile, the heart also showed a relative high Mn content within 1 h after injection. The biodistribution of MMPP in LPS-induced myocardial injury mice was similar to those of healthy mice at 10 min post-injection of MMPP nanoparticles, but the heart maintained a relative high signal intensity and did not decrease obviously at 24 h post-injection (Fig. S2C). Taken together, we speculated that the MMPP could accumulate in the heart, liver and kidney and excreted from the body via both liver and kidneys.

3.4. Biosafety evaluation of MMPP

MMPP has been shown to possess strong ROS scavenging and iron chelating ability *in vitro*, which is expected to become an anti-ferroptosis or anti-inflammatory drug. Since it is mainly distributed in the heart, kidney and liver after transfusion, further tests for biocompatibility and biosafety are needed before its application. We first confirmed that the toxicity of MMPP to H9c2 cells was negligible at different dosages and time by performing MTT assay (Figs. S3A–B). Meanwhile, we intravenously injected MMPP into C57BL/6J mice, and collected major organs and blood samples. H&E staining revealed that no obvious damage was detected in major organs from MMPP-treated group on 1 h, 1 day and 14 days (Fig. 3A). Additionally, liver function and kidney function were evaluated via analyzing serum aspartate transaminase (AST) and alanine transaminase (ALT), urea nitrogen (BUN) and creatinine (CRE) levels, the structure and function of mice hearts were visualized by echocardiography. As showed in Fig. 3B–E and Figs. S3C–E, all test values in the MMPP group were within the normal range and there was no obvious difference compared with the control group. We also found a similar ratio of heart weight to body weight between control and MMPP group (Fig. S3F). These results confirmed the excellent biocompatibility and biosafety of MMPP, which can be considered for clinical application.

3.5. MMPP improved survival and cardiac function in mice with sepsis-induced myocardial injury

To investigate the therapeutic potential of MMPP on sepsis-induced myocardial injury, we established a mouse model of sepsis by intravenous injection of LPS (10 mg/kg body weight) (Fig. 4A). As expected, compared with the LPS group, MMPP treatment significantly increased the survival rate and reduced CK-MB and LDH in serum, suggesting that MMPP might improve mice survival through relieving cardiac injury (Fig. 4B–D). In addition, compared with the control mice, MMPP-treated mice had a slight weight loss after LPS injection and recovered after day 5 (Fig. S4A). Further, we visualized the structure and function of mice hearts by echocardiography after LPS injection. As shown in Fig. 4E–G, LPS led to significant reduction in the ejection fraction (EF) and fractional shortening (FS) compared with those in the control group, indicating that the mice cardiac function was impaired. Notably, MMPP treatment markedly enhanced EF and FS compared with the LPS group. Moreover, there was no difference in the ratio of heart weight to body weight between the three groups (Fig. 4H). H&E staining demonstrated that MMPP treatment has an effective protective effect on sepsis-induced inflammation, hemorrhage and structural disorders (Fig. 4I and Fig. S4B). Taken together, these evidences demonstrated that MMPP could remarkedly alleviate sepsis-induced myocardial injury and improve cardiac function and survival.

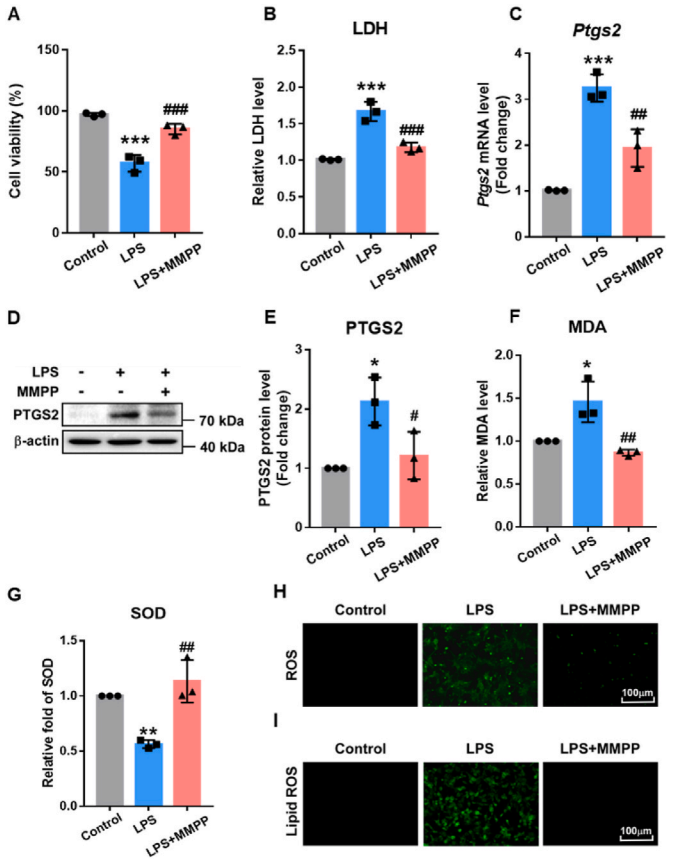

Fig. 6. MMPP inhibited ferroptosis *in vitro* by savaging ROS. A-I. H9c2 cells (A) and neonatal rat cardiomyocytes (B–I) were treated with LPS (10 μg/mL) for 30min, followed by PBS or MMPP nanoparticles treatment (100 μg/mL). Cells were collected after 12h stimulation with LPS. (A) H9c2 cells viability was detected by MTT assay kit. (B) The relative content of LDH in the neonatal rat cardiomyocyte supernatant was measured. (C) The mRNA level of *Ptgs2* gene were examined by RT-PCR. (D–E) Immunoblotting and quantification of PTGS2 were determined. (F–G) The relative levels of MDA and SOD were measured by respective kits. (H) Detection of ROS by DCFH-DA staining (scale bar = 100 μm). (I) Detection of lipid ROS by BODIPY 581/591 C11 staining (scale bar = 100 μm). All images and blots are representative of three independent experiments. All quantitative data are means ± SD of three independent experiments. $*p < 0.05$, $**p < 0.01$, $***p < 0.001$ vs. non-stimulation control group, $\#p < 0.05$, $\#\#p < 0.01$, $\#\#\#p < 0.001$ vs. LPS stimulation control group.

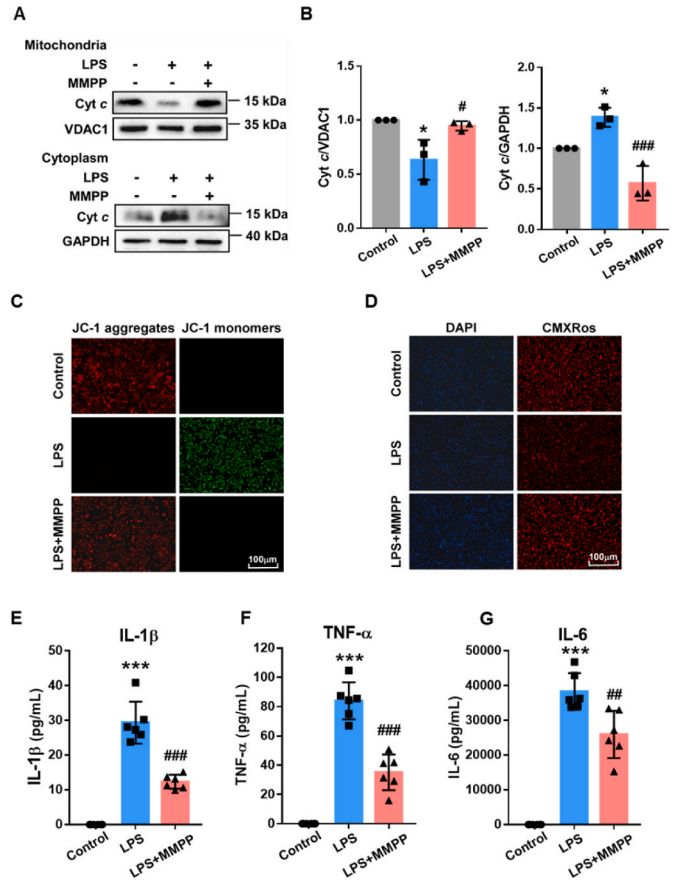

Fig. 7. MMPP protected mitochondrial function and decreased inflammation response. A-D. Neonatal rat cardiomyocytes were treated with LPS (10 μg/mL) for 30min, followed by PBS or MMPP nanoparticles treatment (100 μg/mL). Cells were collected after 12h stimulation with LPS. (A–B) The protein level of Cyt *c* was assessed by Western blot. VDAC1 and GAPDH are markers for mitochondria and cytoplasm, respectively. (C–D) Mitochondrial membrane potentials of neonatal rat cardiomyocytes were examined by JC-1 and CMXRos staining (scale bar = 100 μm). (E–G) The mice serum levels of IL-1β, TNF-a and IL-6 were examined by ELISA (n = 6). All images and blots are representative of three independent experiments. Data are presented as means ± SD. $*p < 0.05$, $***p < 0.001$ vs. non-infection control group, $\#p < 0.05$, $\#\#p < 0.01$, $\#\#\#p < 0.001$ vs. LPS stimulation control group.

3.6. MMPP alleviated sepsis-induced cardiac injury by suppressing ferroptosis through chelating iron

Previous studies have demonstrated that LPS-induced myocardial injury is mainly attributed to ferroptosis, and the expression of PTGS2 is one of the hallmarks of ferroptosis [9,38]. To identify whether MMPP protected cardiac function via suppressing cardiac ferroptosis, we first determined the expression of PTGS2 in heart tissues. As displayed in Fig. 5A–C, compared with the LPS-induced sepsis group, the mRNA and protein levels of PTGS2 were attenuated apparently in the MMPP-treated group. Moreover, LPS challenge increased MDA and decreased SOD in cardiac tissue, whereas MMPP treatment dramatically rescued parameters mentioned above (Fig. 5D and E), suggesting that MMPP could suppress LPS-induced ferroptosis. Since ferroptosis is a type of iron-dependent regulated cell death and our previous data demonstrated that MMPP could chelate free iron. Therefore, we further explored whether MMPP inhibited ferroptosis by chelating iron. Intriguingly, MMPP absolutely mitigated the level of iron in cardiac tissue compared with LPS-sepsis group (Fig. 5F). These data illustrated that MMPP potentially prevent sepsis-induced myocardial injury by suppressing ferroptosis through chelating iron.

3.7. MMPP inhibited ferroptosis in LPS-treated cardiomyocytes through attenuating ROS production

Increasing evidences have shown that ferroptosis is also associated with the accumulation of ROS, and ROS scavengers can entirely inhibit cell ferroptosis [39,40]. Because of the superior antioxidant capacity of MMPP *in vitro* and its ability to accumulate in the heart, we hypothesized that MMPP may also protect cardiomyocytes from oxidative damage and inhibit ferroptosis via attenuating ROS production. To evaluate the role of MMPP in lipid peroxidation, intracellular oxidative damage was firstly investigated in neonatal SD rat cardiomyocytes, H9c2 and AC16 cells. Consistent with *in vivo* experiments, less LPS-related cell damage in MMPP-treated cardiomyocytes exhibited via the increased cell viability and reduced LDH content in culture medium (Fig. 6A and B). Moreover, compared with LPS group, PTGS2 expression was obviously decreased in the MMPP group (Fig. 6C–E and Figs. S5A–C). In addition, higher MDA levels and lower SOD contents were detected in the MMPP group, revealing excellent anti-ferroptosis effect of MMPP on cardiomyocytes (Fig. 6F–G and Fig. S5D). Furthermore, DCFH-DA staining was used to

evaluate the antioxidative effect of MMPP under LPS-induced oxidative stress. As shown in Fig. 6H and Fig. S5E, the stronger green fluorescence was observed in cardiomyocytes stimulated by LPS, suggesting that oxidative damage of cardiomyocytes can be caused by excessive ROS accumulation. In comparison, the green fluorescence in the MMPP treatment group was obviously reduced, suggesting that MMPP played an antioxidant role in septic myocardial injury. Besides, the levels of lipid ROS had decreased in cardiomyocytes pre-treated with MMPP (Fig. 6I and Fig. S5F). These results indicated that MMPP prevented oxidative damage and inhibited ferroptosis of cardiomyocytes through scavenging ROS.

3.8. MMPP protected mitochondrial function and decreased inflammation response

Mitochondria dysfunction is considered to be an early warner of ferroptosis. It has been well established that excessive iron in cells can be taken up by mitochondrial, which leads to promote ROS production by Fenton reactions and induce mitochondria damage [41]. As shown in Fig. 7A and B, MMPP pre-treated cardiomyocytes had attenuated Cytochrome *c* (Cyt *c*) released from the mitochondria to the cytoplasm. It suggested that MMPP protected cardiomyocytes from LPS-induced mitochondrial damage. Meanwhile, JC-1 staining demonstrated that MMPP effectively reduced LPS-induced JC-1 monomers production, indicating that the decrease of mitochondrial membrane potential induced by LPS was hindered (Fig. 7C). Moreover, these results were further verified by Mito Tracker Red CMXRos, in which MMPP treatment maintained mitochondrial function (Fig. 7D). These data supported the idea that MMPP treatment attenuated mitochondrial dysfunction and damage induced by LPS. Cardiomyocytes inflammatory response is also one of the most important pathological changes in myocardial injury and may in turn drive mitochondrial ROS generation and aggravation of ferroptosis. Interestingly, we found that MMPP could markedly alleviate inflammation response by inhibiting LPS-induced the production of inflammatory cytokines including IL-1β, TNF-a and IL-6, exhibiting great anti-inflammation potential therapy (Fig. 7E–G and Figs. S6A–C). Collectively, these results confirmed that MMPP could effectively attenuate the sepsis-induced myocardial injury due to its excellent anti-ferroptosis and anti-inflammation effects.

4. Conclusion

In the present study, we successfully synthesized melanin-like nanoparticles and found that MMPP could accumulate in the heart, especially after LPS-induced injury. We demonstrated for the first time the therapeutic effect of melanin-like nanoparticles as a cardioprotective agent to alleviate sepsis-induced myocardial injury. We performed *in vitro* and *in vivo* experiments and uncovered that MMPP treatment could effectively inhibit cardiomyocytes ferroptosis by scavenging ROS and preventing iron accumulation. Importantly, injectable MMPP could effectively protect mice from LPS-induced lethal sepsis and improve cardiac function. Inflammation is a double-edged sword, not only protecting against bacterial invasion, but also causing tissue damage. We observed that MMPP strongly attenuated inflammatory cytokines production and alleviated oxidative stress-triggering cardiac injury. Taken together, our findings suggest that MMPP has promising efficacy in the treatment of sepsis-induced myocardial injury, which needs further confirmation by clinical translational studies in future.

Ethics approval and consent to participate

All animal experiments were approved by the Experimental Animal Ethics Committee of Tianjin Medical University.

CRediT authorship contribution statement

Chang Liu: Investigation, Methodology, Data curation, Writing – original draft, Funding acquisition. **Quan Zou:** Investigation, Methodology, Data curation, Writing – original draft. **Huixin Tang:** Investigation, Methodology, Data curation. **Jia Liu:** Investigation. **Shiqi Zhang:** Investigation. **Caihong Fan:** Investigation. **Junwei Zhang:** Investigation. **Ruiqing Liu:** Investigation. **Yashan Liu:** Investigation. **Ruiyan Liu:** Investigation. **Yan Zhao:** Investigation. **Qiang Wu:** Validation. **Zhi Qi:** Conceptualization, Project administration, Writing – review & editing, Funding acquisition. **Yanna Shen:** Conceptualization, Project administration, Writing – review & editing, Funding acquisition.

Declaration of competing interest

The authors declare that they have no known competing financial interests or personal relationships that could have appeared to influence the work reported in this paper.

Acknowledgments

This work was supported by grants of the National Natural Science Foundation of China to YS (82272221, 32071263), ZQ (81971887, 82172170) and CL (82202403); the Tianjin Natural Science Foundation to ZQ (20JCYBJC01260, 20JCYBJC01230); the Key Laboratory of Emergency and Trauma (Hainan Medical University), Ministry of Education to YS (KLET-202018); the Fundamental Research Funds for the Central Universities, Nankai University to ZQ (63211140); the Scientific Research Project of Tianjin Education Commission to CL (2020KJ206); National College Students' Innovative Entrepreneurial Training Plan Program to RL (202210062001).

Appendix A. Supplementary data

Supplementary data to this article can be found online at https://doi.org/10.1016/j.bioactmat.2022.12.026.

References

[1] T. Honda, Q. He, F. Wang, A.N. Redington, Acute and chronic remote ischemic conditioning attenuate septic cardiomyopathy, improve cardiac output, protect systemic organs, and improve mortality in a lipopolysaccharide-induced sepsis model, Basic Res. Cardiol. 114 (3) (2019) 15.
[2] M. L'Heureux, M. Sternberg, L. Brath, J. Turlington, M.G. Kashiouris, Sepsis-induced cardiomyopathy: a comprehensive review, Curr. Cardiol. Rep. 22 (5) (2020) 35.
[3] S.M. Hollenberg, M. Singer, Pathophysiology of sepsis-induced cardiomyopathy, Nat. Rev. Cardiol. 18 (6) (2021) 424–434.
[4] A. Vieillard-Baron, V. Caille, C. Charron, G. Belliard, B. Page, F. Jardin, Actual incidence of global left ventricular hypokinesia in adult septic shock, Crit. Care Med. 36 (6) (2008) 1701–1706.
[5] M. Storgaard, J. Hallas, B. Gahrn-Hansen, S.S. Pedersen, C. Pedersen, A.T. Lassen, Short- and long-term mortality in patients with community-acquired severe sepsis and septic shock, Scand. J. Infect. Dis. 45 (8) (2013) 577–583.
[6] Y. Wang, Y. Wang, D. Yang, et al., β1-adrenoceptor stimulation promotes LPS-induced cardiomyocyte apoptosis through activating PKA and enhancing CaMKII and IκBα phosphorylation, Crit. Care 19 (1) (2015) 76.
[7] Y. Sun, X. Yao, Q.J. Zhang, et al., Beclin-1-Dependent autophagy protects the heart during sepsis, Circulation 138 (20) (2018) 2247–2262.
[8] N. Li, H. Zhou, H. Wu, et al., STING-IRF3 contributes to lipopolysaccharide-induced cardiac dysfunction, inflammation, apoptosis and pyroptosis by activating NLRP3, Redox Biol. 24 (2019), 101215.
[9] N. Li, W. Wang, H. Zhou, et al., Ferritinophagy-mediated ferroptosis is involved in sepsis-induced cardiac injury, Free Radic. Biol. Med. 160 (2020) 303–318.
[10] A. Belavgeni, C. Meyer, J. Stumpf, C. Hugo, A. Linkermann, Ferroptosis and necroptosis in the kidney, Cell Chem. Biol. 27 (4) (2020) 448–462.
[11] T. Dong, D. Liao, X. Liu, X. Lei, Using small molecules to dissect non-apoptotic programmed cell death: necroptosis, ferroptosis, and pyroptosis, Chembiochem : Eur. J. Chem. Biol. 16 (18) (2015) 2557–2561.
[12] X. Fang, H. Wang, D. Han, et al., Ferroptosis as a target for protection against cardiomyopathy, Proc. Natl. Acad. Sci. U. S. A 116 (7) (2019) 2672–2680.
[13] T.J. Park, J.H. Park, G.S. Lee, et al., Quantitative proteomic analyses reveal that GPX4 downregulation during myocardial infarction contributes to ferroptosis in cardiomyocytes, Cell Death Dis. 10 (11) (2019) 835.

[14] B. Liu, C. Zhao, H. Li, X. Chen, Y. Ding, S. Xu, Puerarin protects against heart failure induced by pressure overload through mitigation of ferroptosis, Biochem. Biophys. Res. Commun. 497 (1) (2018) 233–240.
[15] B.R. Stockwell, J.P. Friedmann Angeli, H. Bayir, et al., Ferroptosis: a regulated cell death nexus linking metabolism, redox biology, and disease, Cell 171 (2) (2017) 273–285.
[16] Y. Tan, H. Ouyang, X. Xiao, J. Zhong, M. Dong, Irisin ameliorates septic cardiomyopathy via inhibiting DRP1-related mitochondrial fission and normalizing the JNK-LATS2 signaling pathway, Cell Stress & Chaperones 24 (3) (2019) 595–608.
[17] B. Haileselassie, R. Mukherjee, A.U. Joshi, et al., Drp1/Fis1 interaction mediates mitochondrial dysfunction in septic cardiomyopathy, J. Mol. Cell. Cardiol. 130 (2019) 160–169.
[18] W. Chang, M. Feng, Y. Li, Y. Sun, L. Sun, MKP1 overexpression reduces TNF-α-induced cardiac injury via suppressing mitochondrial fragmentation and inhibiting the JNK-MIEF1 pathways, J. Cell. Physiol. 234 (2019) 16148–16159.
[19] C. Nedeva, J. Menassa, H. Puthalakath, Sepsis: inflammation is a necessary evil, Front. Cell Dev. Biol. 7 (2019) 108.
[20] M. Trinder, J.H. Boyd, L.R. Brunham, Molecular regulation of plasma lipid levels during systemic inflammation and sepsis, Curr. Opin. Lipidol. 30 (2) (2019) 108–116.
[21] H. Zhao, H. Chen, M. Xiaoyin, et al., Autophagy activation improves lung injury and inflammation in sepsis, Inflammation 42 (2) (2019) 426–439.
[22] Q. Jiang, Z. Luo, Y. Men, et al., Red blood cell membrane-camouflaged melanin nanoparticles for enhanced photothermal therapy, Biomaterials 143 (2017) 29–45.
[23] M. Chu, W. Hai, Z. Zhang, et al., Melanin nanoparticles derived from a homology of medicine and food for sentinel lymph node mapping and photothermal in vivo cancer therapy, Biomaterials 91 (2016) 182–199.
[24] D.W. Zheng, S. Hong, L. Xu, et al., Hierarchical micro-/nanostructures from human hair for biomedical applications, Adv. Mater. 30 (27) (2018), e1800836.
[25] Q. Jiang, Y. Liu, R. Guo, et al., Erythrocyte-cancer hybrid membrane-camouflaged melanin nanoparticles for enhancing photothermal therapy efficacy in tumors, Biomaterials 192 (2019) 292–308.
[26] J. Li, X. Liu, Z. Zhou, et al., Lysozyme-assisted photothermal eradication of methicillin-resistant Staphylococcus aureus infection and accelerated tissue repair with natural melanosome nanostructures, ACS Nano 13 (10) (2019) 11153–11167.
[27] Y. Liu, K. Ai, X. Ji, et al., Comprehensive insights into the multi-antioxidative mechanisms of melanin nanoparticles and their application to protect brain from injury in ischemic stroke, J. Am. Chem. Soc. 139 (2) (2017) 856–862.
[28] X. Bao, J. Zhao, J. Sun, M. Hu, X. Yang, Polydopamine nanoparticles as efficient scavengers for reactive oxygen species in periodontal disease, ACS Nano 12 (9) (2018) 8882–8892.
[29] H. Zhao, Z. Zeng, L. Liu, et al., Polydopamine nanoparticles for the treatment of acute inflammation-induced injury, Nanoscale 10 (15) (2018) 6981–6991.
[30] T. Sun, D. Jiang, Z.T. Rosenkrans, et al., A melanin-based natural antioxidant defense nanosystem for theranostic application in acute kidney injury, Adv. Funct. Mater. 29 (48) (2019), 1904833.
[31] A. Jin, Y. Wang, K. Lin, L. Jiang, Nanoparticles modified by polydopamine: working as "drug" carriers, Bioact. Mater. 5 (3) (2020) 522–541.
[32] H. Lee, S.M. Dellatore, W.M. Miller, P.B. Messersmith, Mussel-inspired surface chemistry for multifunctional coatings, Science 318 (5849) (2007) 426–430.
[33] Z. Dong, H. Gong, M. Gao, et al., Polydopamine nanoparticles as a versatile molecular loading platform to enable imaging-guided cancer combination therapy, Theranostics 6 (7) (2016) 1031–1042.
[34] Z. Li, B. Wang, Z. Zhang, et al., Radionuclide imaging-guided chemo-radioisotope synergistic therapy using a (131)I-labeled polydopamine multifunctional nanocarrier, Mol. Ther. : J. Am. Soc. Gene Ther. 26 (5) (2018) 1385–1393.
[35] Y. Dai, D. Yang, D. Yu, et al., Mussel-Inspired polydopamine-coated lanthanide nanoparticles for NIR-II/CT dual imaging and photothermal therapy, ACS Appl. Mater. Interfaces 9 (32) (2017) 26674–26683.
[36] S. Yao, X. Li, J. Liu, Y. Sun, Z. Wang, Y. Jiang, Maximized nanodrug-loaded mesenchymal stem cells by a dual drug-loaded mode for the systemic treatment of metastatic lung cancer, Drug Deliv. 24 (1) (2017) 1372–1383.
[37] C. Liu, S. Huang, X. Wang, et al., The otubain YOD1 suppresses aggregation and activation of the signaling adaptor MAVS through lys63-linked deubiquitination, J. Immunol. 202 (10) (2019) 2957–2970. : 1950.
[38] S.H. Huang, M. Xu, H.M. Wu, et al., Isoquercitrin attenuated cardiac dysfunction via AMPKα-dependent pathways in LPS-treated mice, Mol. Nutr. Food Res. 62 (24) (2018), e1800955.
[39] E. Park, S.W. Chung, ROS-mediated autophagy increases intracellular iron levels and ferroptosis by ferritin and transferrin receptor regulation, Cell Death Dis. 10 (11) (2019) 822.
[40] N. Wang, H. Ma, J. Li, et al., HSF1 functions as a key defender against palmitic acid-induced ferroptosis in cardiomyocytes, J. Mol. Cell. Cardiol. 150 (2021) 65–76.
[41] S. Wei, T. Qiu, X. Yao, et al., Arsenic induces pancreatic dysfunction and ferroptosis via mitochondrial ROS-autophagy-lysosomal pathway, J. Hazard Mater. 384 (2020), 121390.